

## Chapter 4

# Electrical Properties of Graphene Wrinkles and Nanoribbons

Part of the contents presented in this chapter are based on Xu, K., Cao, P.G. and Heath, J.R. "Scanning tunneling microscopy characterization of the electrical properties of wrinkles in exfoliated graphene monolayers," *Nano Lett*, 9, 4446-4451 (2009). (Ref.<sup>1</sup>)

### 4.1 Introduction

Graphene refers to a monolayer of carbon atoms tightly packed into a two-dimensional (2D) honeycomb lattice. The discovery of graphene in an isolated state<sup>2, 3</sup> has generated widespread research interest.<sup>4-6</sup> The linear dispersion spectrum of graphene causes its charge carriers to behave like massless Dirac fermions, leading to various novel electrical properties that are of fundamental interest. Meanwhile, the unique structure of graphene, in which all atoms are surface atoms, makes its electronic band structure and hence electrical properties extremely sensitive to size effects, surface curvatures, as well as environmental interactions.

#### 4.1.1 Wrinkles in graphene

Graphene initially appeared to be a strictly 2D electronic system, and quantum Hall effects were observed in graphene up to room temperature.<sup>7</sup> On the other hand,

theory has predicted that strictly 2D crystals are thermodynamically unstable and therefore should not exist at any finite temperature.<sup>8</sup>

This contradiction was reconciled by recent transmission electron microscopy (TEM) studies on suspended graphene, in which a microscopically corrugated three-dimensional structure was revealed,<sup>9,10</sup> overturning the naïve picture of graphene being a flat 2D crystal. The <1 nm local corrugations (“ripples”) discovered in these TEM studies are believed to be intrinsic,<sup>11</sup> and so are important for understanding graphene electrical properties.<sup>5,12-16</sup> The low resolution of TEM, especially in the vertical direction, however, limits further detailed studies of these corrugations, and how those corrugations can influence the graphene properties. In addition, the structure and properties of suspended graphene may be fundamentally different from graphene deposited on SiO<sub>2</sub> substrates, the most widely studied form of graphene.

Scanning tunneling microscopy (STM) provides a valuable alternative, which probes morphology and electrical properties at atomic resolution in all three dimensions. Atomically resolved STM topographs of graphene on SiO<sub>2</sub> substrates have been reported,<sup>17-21</sup> from which the height of graphene ripples was determined to be 3-5 Å. Meanwhile, attempts to correlate local electrical properties with the observed ripples have achieved only limited success.<sup>21-23</sup>

In this chapter, we report on the STM study of a new class of corrugations in monolayer graphene sheets that have been largely neglected in previous studies, i.e., wrinkles ~10 nm in width and ~3 nm in height. We found such corrugations to be ubiquitous in graphene, and have distinctly different properties in comparison to other

regions of graphene that only contain small ripples. In particular, a “three-for-six” triangular pattern of atoms is exclusively and consistently observed on wrinkles, suggesting the local curvature of the wrinkle is a perturbation that breaks the six-fold symmetry of the graphene lattice. Through scanning tunneling spectroscopy (STS), we further demonstrate that the wrinkles have lower electrical conductance when compared to other regions of graphene, and are characterized by the presence of midgap states, which is in agreement with recent theoretical predictions. Our results suggest that, in addition to the previously investigated, low-amplitude ripples, these larger wrinkles likely play an important role in determining the electrical properties of graphene sheets.

#### **4.1.2 Graphene nanoribbons**

Although graphene has drawn tremendous attention for studies of its fundamental structural and electronic properties in recent years, the absence of an energy gap in graphene poses a challenge for conventional semiconductor field-effect transistor (FET) device operations.<sup>24</sup> Previous studies have shown that an energy gap can be opened up by patterning graphene into ribbons ~10 nm in width.<sup>25-28</sup> This is explained in terms of a quantum size effect, where the initially 2D carriers are confined into a 1D system.

Experimentally, individual graphene nanoribbons (GNRs) have been fabricated through conventional e-beam lithography (EBL) and individually addressed for transport measurement characterizations.<sup>29, 30</sup> However, the measurement results often vary from sample to sample due to the disorders introduced along the GNR edges during the lithography process. The origin of the energy gap is therefore complicated in this situation. Various theoretical scenarios, including, for example, Coulomb blockade in a series of quantum dots<sup>31</sup> and edge disorder-induced Anderson localization<sup>32</sup> have been

invoked to explain the observed large sample variations. Large number of GNRs fabricated in parallel could in overall average out the edge variations and give more consistent results. To our knowledge, such parallel GNR arrays have not been investigated due to the difficulties involved in the fabrication process.

In the remainder of this chapter, we describe our studies on high-density parallel GNR arrays, with the aim of elucidating the effects of GNR width and number of graphene layers on the formation of energy gaps in GNRs. Electron transport in all of our GNR devices exhibits thermally activated behavior, regardless of number of layers: conductance decreases with decreasing temperature. This contrasts with the behavior in “bulk” graphene film, the conductance of which generally increases as temperature decreases.<sup>25</sup> Due to the measurement of large numbers of parallel GNRs (~80) at once in our study, variations observed previously on individual GNR devices are averaged out in our studies. Therefore, we have observed smoother and more consistent development of the depressed conductance region versus gate voltage as temperature decreases. More importantly, we have also for the first time clearly observed how the properties of GNRs evolve as a function of the number of graphene layers, while fixing the width of GNRs to be exactly the same. We found the band gap (and so the on-off ratio) decreases as the number of layers increases. These results suggest that, in addition to single layer graphene, GNRs of different thicknesses can also be harnessed as different building blocks for engineering GNRs for FET applications.

## 4.2 Experimental

### 4.2.1 Fabrication of graphene sheets

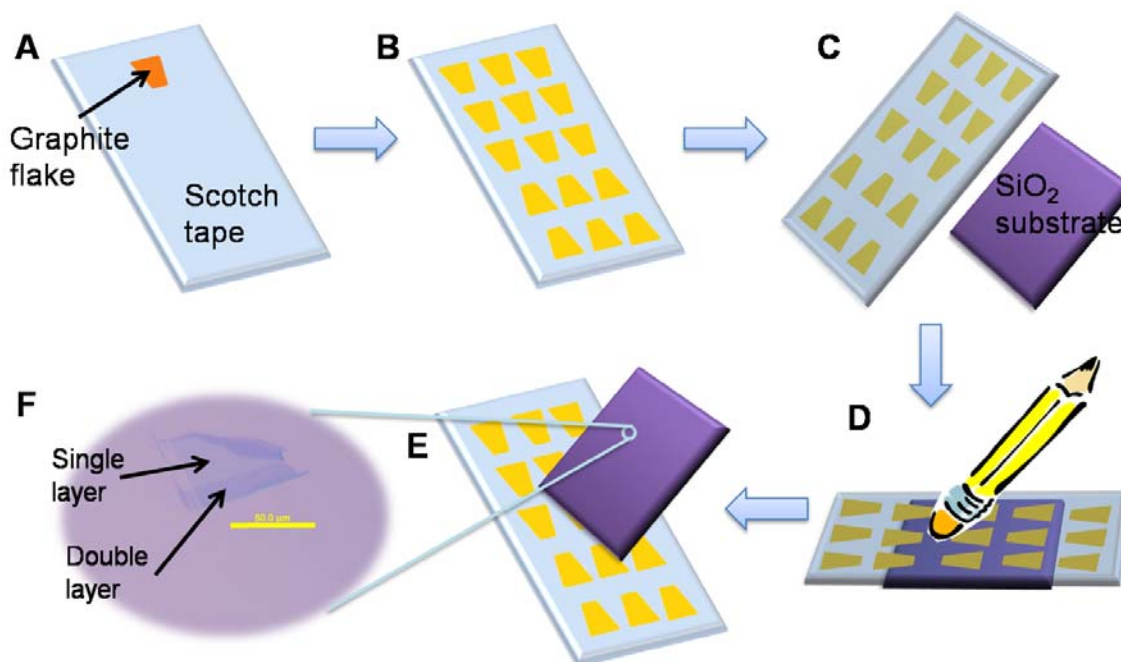


**Figure 4.1. Process flow schematics for the fabrication of graphene sheets.** (A): A thin Kish graphite flake is stuck onto Scotch tape. (B): By folding and peeling the tape ~10 times, the graphite flake is exfoliated into multiple thinner flakes, covering the entire tape surface. (C): The Scotch tape is turned over, and the graphite flakes on the surface are brought into contact with a freshly cleaned SiO<sub>2</sub> substrate. (D): An eraser is used to rub the back of the tape, to ensure close contact between the graphite flakes and the substrate. (E): The Scotch tape is peeled off from the substrate, leaving graphene sheets and other thin graphitic layers on the SiO<sub>2</sub> substrate. (F): Graphene sheets on the surface are identified through an optical microscope. Single-layer and double-layer parts of the graphene sheet (as confirmed through spatially resolved Raman spectroscopy) are labeled on graph. Scale bar: 50 μm.

The monolayer graphene sheets investigated in this study were fabricated on insulating SiO<sub>2</sub> substrates through mechanical exfoliation of Kish graphite flakes.<sup>3,33</sup> The detailed process flow is presented in Figure 4.1. It should be noted that this process is time-consuming and low-yielding, and the locations of the resultant graphene sheets are uncontrolled.

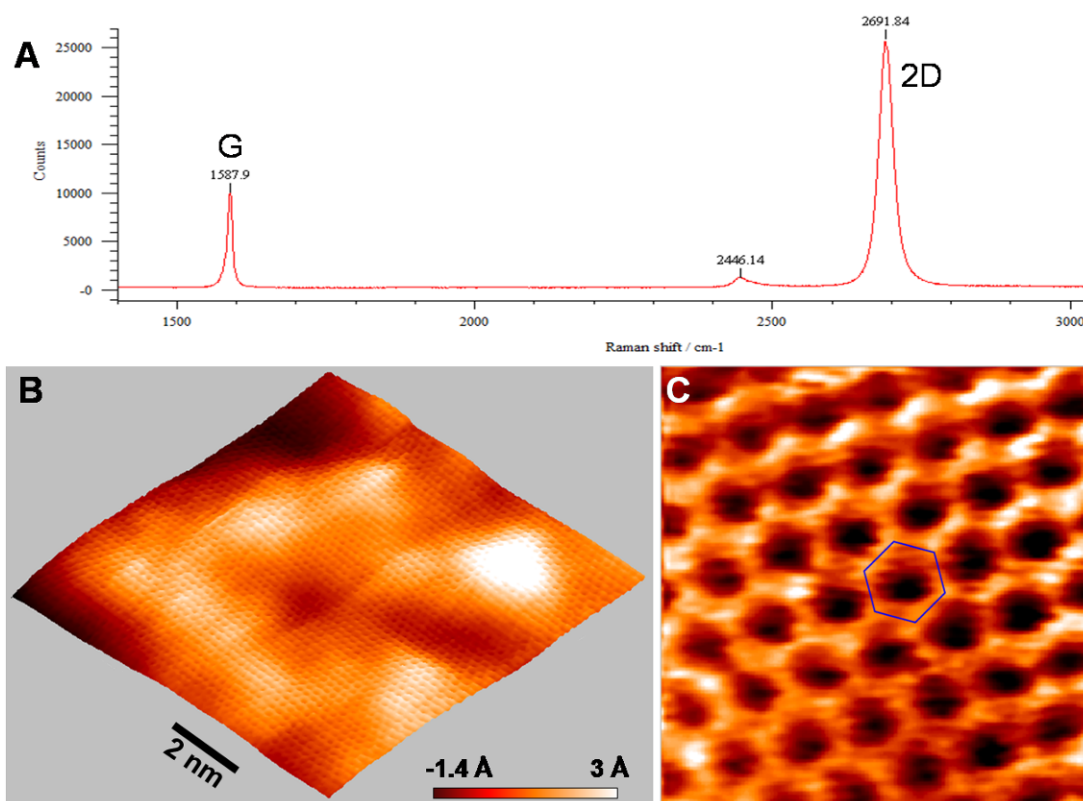


**Figure 4.2. Raman spectrum and STM topography of a typical graphene sample.** (A): Raman spectrum of the graphene sample. (B): Atomically resolved constant-current STM topography ( $V_b = 0.5$  V,  $I = 0.22$  nA) of the graphene sample. (C): A close-up of the honeycomb lattice. The blue hexagon has sides of 1.42 Å.

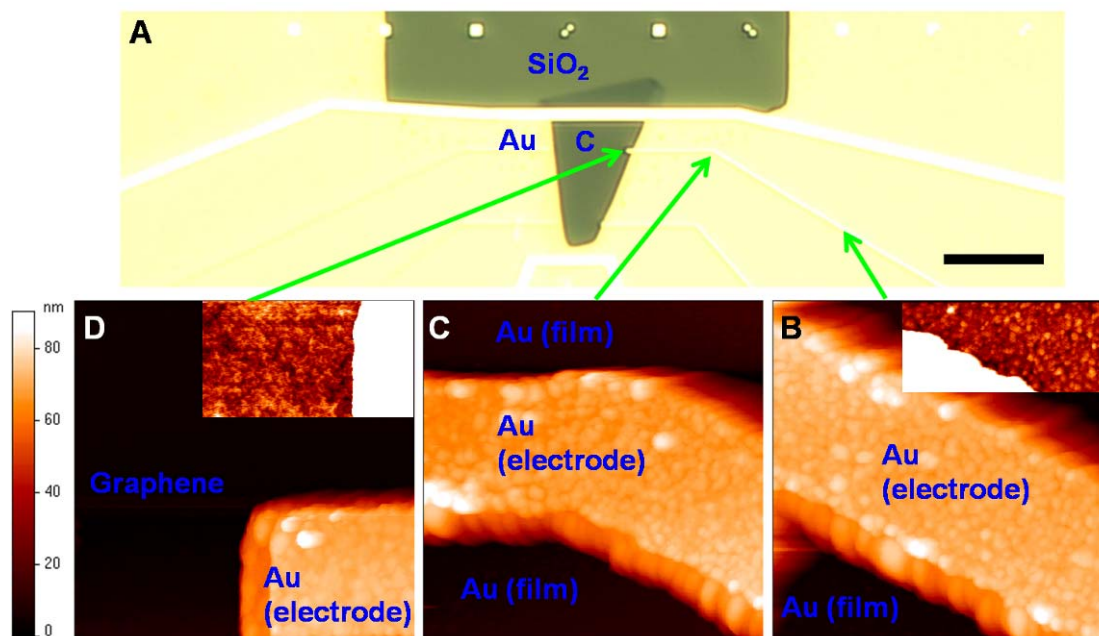
Monolayer graphene sheets  $\sim 20$   $\mu\text{m}$  in size were optically identified, and unambiguously confirmed through spatially resolved Raman spectroscopy. As shown in

Figure 4.2A, a symmetric single peak is observed at  $\sim 2700\text{ cm}^{-1}$  (2D band) in the Raman spectrum, and the peak height is larger than the G band at  $\sim 1580\text{ cm}^{-1}$ . Both features are characteristic of pristine monolayer graphene sheets.<sup>34,35</sup> Ti/Au electrodes were contacted to the fabricated graphene sheets using electron-beam lithography, and Hall measurements revealed room-temperature carrier mobilities of  $>6,000\text{ cm}^2/\text{Vs}$ , which is typical of high-quality graphene at room temperature.<sup>4</sup>

For STM measurements, the graphene sheets were then contacted at all edges with gold, so that the tunneling current diffused in-plane through the gold film. The electrodes defined in the previous step served as guides for locating the graphene sheets using STM (Figure 4.3). As in previous chapters, STM studies were performed using an Omicron low-temperature UHV STM system with mechanically cut Pt/Ir tips. All STM data were taken at liquid nitrogen (77 K) or liquid helium (4 K) temperatures, and a vacuum of better than  $10^{-10}$  Torr was maintained during experiment.

#### **4.2.2 Fabrication of graphene nanoribbons**

Our GNR devices were prepared using a superlattice nanowire pattern (SNAP) transfer technique.<sup>36</sup> SNAP uses a template consisting of alternating layers of GaAs/ $\text{Al}_x\text{Ga}_{(1-x)}\text{As}$ , which is grown by molecular-beam epitaxy (MBE) on top of GaAs wafers, for nanowire (NW) patterning. Through selective etching of either GaAs or  $\text{Al}_x\text{Ga}_{(1-x)}\text{As}$ , layer thickness can be translated to the nanowire width. In principle, this width can be as thin as a few atomic layers since MBE is capable of growing with atomic resolution.



**Figure 4.3. Locating the graphene sheet in STM.** STM only works for conducting surfaces. To prevent the STM tip from crashing into the sample, it's essential to avoid scanning over insulating surfaces, including the  $\text{SiO}_2$  substrate used in this study. On the other hand, positioning of the STM tip under optical microscope has poor location control ( $\sim 100 \mu\text{m}$ ). This obstacle can be overcome by following the method described here. **(A)**: An optical microscope image of a graphene device for STM study. Graphene is labeled as "C" for carbon. Scale bar:  $10 \mu\text{m}$ . The graphene sheet is contacted at all edges with gold, so that the tunneling current diffuses in-plane through the gold film. Under optical microscope, the STM tip can be easily positioned on the conductive gold film ( $\sim 500 \mu\text{m} \times 500 \mu\text{m}$ ). **(B)-(C)**: STM topographs ( $800 \text{ nm} \times 800 \text{ nm}$ ) demonstrating how the graphene sheet is located for STM imaging. Large scale ( $\sim 2 \mu\text{m}$ ) scans are first performed to find the raised electrodes in the Au film. The graphene sheet is then located by tracing the electrodes. **(B)**: Topograph of an electrode when the tip is far from graphene. Inset shows the topograph of the gold film near the electrode (white) with a 5 nm height scale: At this scale nanoscale gold islands are clearly observed. **(C)**: By tracing along the electrode, the tip is moved closer to graphene, and the turn in the electrode unequivocally identifies the tip position on the gold film. **(D)**: Topograph obtained at the end of the electrode, where the graphene sheet is reached [cf. (A)]. Inset shows the topograph of the graphene sheet near the electrode (white) on a small (2 nm) height scale: ripples in the graphene are observed.

Figure 4.4 shows representative optical images, illustrating the fabrication process. A thin layer of  $\text{SiO}_2$  (~10 nm) was first deposited onto a graphene sheet resting on 300 nm  $\text{SiO}_2/\text{Si}$  substrate (Figure 4.4ab). This is to protect graphene from being etched away during the following reactive ion etching (RIE) steps. A template of an array of metal nanowires (for example, Pt) was then stamped onto and securely bonded to the surface (Figure 4.4c) with a thin layer of epoxy (EpoxyBond 110, Allied High Tech, Rancho Dominguez, CA). The NW array was obtained by e-beam evaporation of Pt onto the raised edges of a differentially etched edge of a  $\text{GaAs}/\text{Al}_x\text{Ga}_{(1-x)}\text{As}$  superlattice wafer (IQE, Cardiff, UK).<sup>36</sup> In this way, the atomic control over the film thicknesses of the superlattice stack was translated into control over the width and spacing of NWs. The superlattice and extra exposed epoxy were then removed via selective wet and RIE etch, respectively (Figure 4.4d).

Before the NW patterns were transferred into the underlying graphene film, EBL was used to define a 50 nm thick  $\text{Al}_2\text{O}_3$  mask for the monolithic contact electrodes (Figure 4.4e). After pattern transfer (Figure 4.4f) and removal of the mask (Figure 4.4g), the so-defined large blocks of graphene (>500 nm in width) were then contacted by Ti/Au electrodes (Figure 4.4h). An advantage of this contact by larger areas of graphene is that the Schottky barrier formation by metal electrodes is absent. The top platinum nanowires and the protecting  $\text{SiO}_2$  layer over the nanoribbons are not removed in the following transport measurements and in some cases, the platinum nanowires can be employed as a top gate.

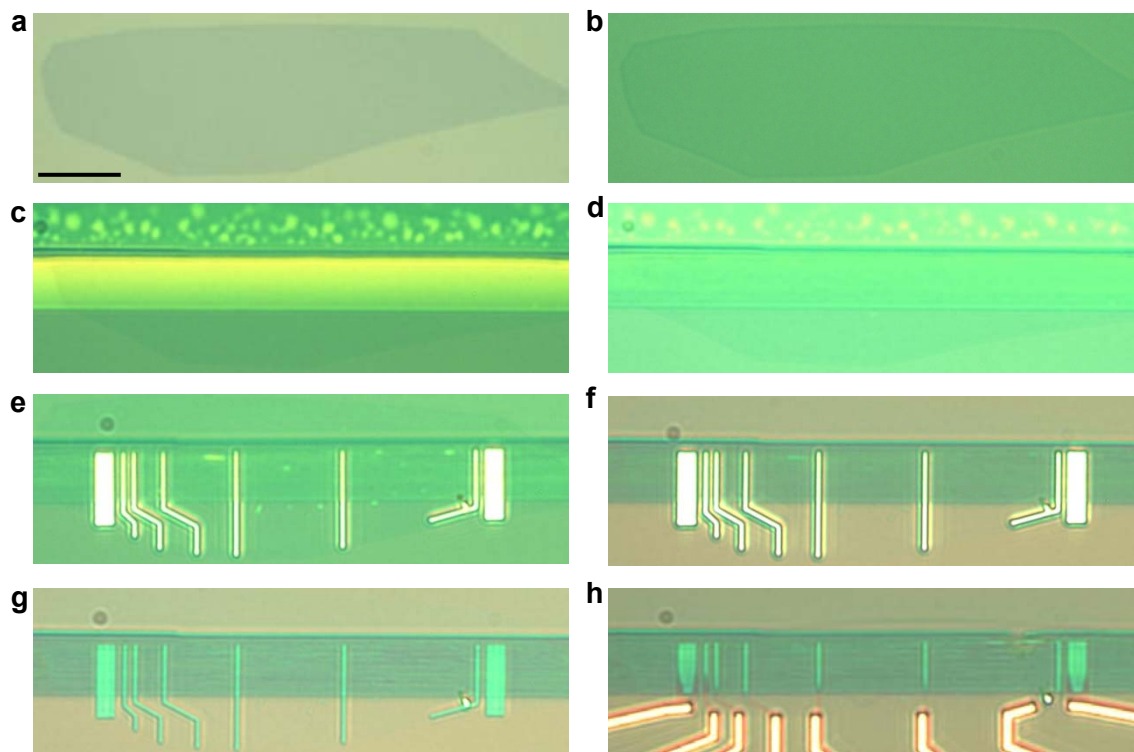


**Figure 4.4. Representative bright-field optical images following the GNR fabrication process.** (a) Exfoliated graphene on 300 nm SiO<sub>2</sub>/Si substrate. (b) Evaporation of 18 nm SiO<sub>2</sub> protection layer, covering both graphene and substrate. (c) Stamping of SNAP Pt nanowires onto graphene via epoxy bonding. (d) Extra epoxy in between nanowires removed by RIE in a 40 MHz Unaxis SLR parallel-plate RIE system ~5 min with O<sub>2</sub> (10 sccm, 5 mTorr, 40 W). (e) Evaporation of 50 nm thick Al<sub>2</sub>O<sub>3</sub> mask to define the monolithic contacts. Spacings between the masks were adjusted so as to define GNRs of different lengths (ranging from 0.5 to ~50 μm) but of the same width. (f) Both nanoribbon and electrode patterns were transferred into the graphene film. Exposed SiO<sub>2</sub> and underlying graphene (not protected by Al<sub>2</sub>O<sub>3</sub> mask and Pt nanowires) were removed sequentially by highly directional RIE with ~4 min CF<sub>4</sub>/He (20/30 sccm, 5 mTorr, 40 W) and with ~2 min O<sub>2</sub> plasma (10 sccm, 5 mTorr, 40W). (g) Al<sub>2</sub>O<sub>3</sub> Mask removed by ~30 minutes in 10% H<sub>3</sub>PO<sub>4</sub> + 90% H<sub>2</sub>O. (h) Evaporation of Ti/Au (20/200 nm) to make metal contacts. The scale bar is 10 μm and applies for all images.

The conductance of GNRs was measured using a standard lock-in technique. A low-noise function generator (DS360, Stanford Research System) was used to supply an AC signal (100  $\mu$ V at 11 Hz) to the device and the output signal was fed into a lock-in amplifier (SR830, Stanford Research System). The time constant and slope used in the experiments were 300 ms and 12 dB, respectively. The heavily doped silicon substrate below the 300 nm SiO<sub>2</sub> served as a bottom gate electrode to tune the carrier density in the GNRs. The gate voltages were supplied by a Keithley 2400 source meter. Temperature-dependent experiments were carried out in a SQUID cryostat (MPMS-XL, Quantum Design, CA). A program written with Labview 7.1 was used to control the operations.

### **4.3 Structural and electrical characterizations of graphene wrinkles**

Figure 4.2B gives the constant-current STM topograph obtained from a typical graphene device. Atomically resolved, clear honeycomb structures were observed for all samples, with bond lengths in agreement with the known graphene lattice constant (Figure 4.2C). The same honeycomb structures are obtained independent of the specific parameters used for imaging.

No lattice defects were ever observed during our atomically resolved STM study over an accumulated area of  $\sim 10^4$  nm<sup>2</sup> on different samples, corresponding to  $>10^5$  atoms. This is in agreement with the measured high carrier mobilities, but in contrast with STM results obtained on graphene epitaxially grown on conductive substrates, in which lattice defects are observed at the nanometer scale.<sup>37</sup> Surface corrugations (ripples) of  $\sim 4$  Å in height are observed for most regions of our graphene samples (Figure 4.2B), in agreement with previous studies.<sup>17-21</sup>

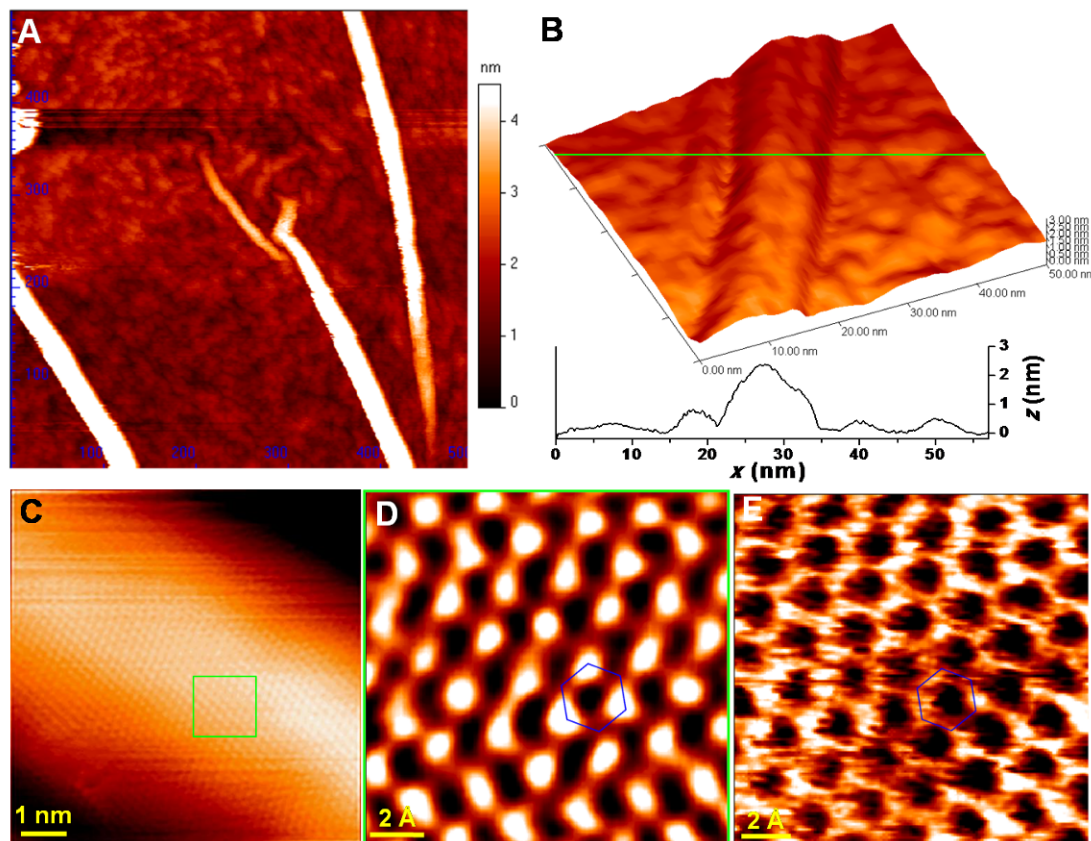


**Figure 4.5. STM topographs of graphene wrinkles.** (A): A large-area (500 nm by 500 nm) scan of wrinkles in a graphene sheet. A small color scale is used to accentuate the coexisting small ripples. The largest height in this topograph is  $\sim 6$  nm. (B): A three-dimensional plot of the topograph of a typical wrinkle structure. The coexisting ripple structures are also observed. A height profile through the green line is given. (C): Atomically resolved topograph obtained on the top of the wrinkle. Scale bar: 1 nm. (D): A close-up of the observed “three-for-six” triangular pattern on the wrinkle, corresponding to the green square in (C). Scale bar: 2 Å. The blue hexagon has sides of 1.42 Å, corresponding to the size of one hexagonal carbon ring. (E): Atomically resolved topograph taken right next to the wrinkle, on a “flat” region of the same graphene sheet. Scale bar: 2 Å. The blue hexagon has sides of 1.42 Å.

In addition to the previously observed ripples, we also frequently encounter larger-amplitude wrinkle-like structures that are 5 to 20 nm in width, 2 to 5 nm in height, and have lengths from  $\sim 100$  nm to  $\sim 1$   $\mu\text{m}$ . Figure 4.5A presents the topograph obtained from a region of a graphene sample in which multiple wrinkles are observed. The wrinkles appear to be continuous parts of the graphene sheet that buckle up from the underlying substrate (Figure 4.5B), reminiscent of wrinkles that spontaneously occur in thin elastic sheets under stress.<sup>38</sup> However, quite different from a conventional thin sheet, the observed graphene wrinkles are found to be accompanied (both on and near the wrinkles) by the  $\sim 4$  Å small ripples that are known to be intrinsic<sup>11</sup> to graphene (Figure 4.5B).

Wrinkle-like structures have been seen before in TEM images of suspended graphene sheets<sup>34</sup> and in STM and high-resolution scanning electron microscope (SEM) images of graphene grown on conducting substrates,<sup>39,40</sup> but their structure and properties have not been carefully characterized. Moreover, wrinkles were not previously known to be present in the high-mobility, mechanically exfoliated graphene sheets on  $\text{SiO}_2$  substrates, presumably due to their low occurrence rate and small physical dimensions: features with such dimensions are hard to detect optically, or with an SEM or atomic force microscope. High-resolution STM topographs were only recently achieved for graphene sheets on insulating substrates.<sup>17-21</sup>

The wrinkle structures were found to be ubiquitous on exfoliated graphene sheets on  $\text{SiO}_2$ . Wrinkles appear randomly across the sheets, and one or more wrinkles are typically observed when the scanning area is larger than  $\sim 2$   $\mu\text{m}^2$ . Previous STM studies have indicated that wrinkles of similar physical dimensions appear at a similar density on

freshly cleaved graphite surfaces obtained through mechanical exfoliation using adhesive tapes.<sup>41</sup> Because a similar exfoliation technique is employed in the fabrication of graphene sheets,<sup>3, 33</sup> it may be that wrinkles are unavoidable for graphene on SiO<sub>2</sub>. Recent theoretical studies have also proposed the spontaneous formation of wrinkles for graphene on SiO<sub>2</sub> substrates.<sup>42</sup> We, however, do not dismiss the possibility that the standard microfabrication procedures employed in this study might result in additional wrinkles in the graphene sheet.

Surprisingly, atomically resolved topographs (Figure 4.5C, D) reveal very different structures for the wrinkles in comparison with other parts of graphene. A triangular pattern is observed over the entire graphene wrinkle (Figure 4.5C, D), and the distance between adjacent bright spots is  $\sim 2.5$  Å, indicating the honeycomb six-fold symmetry of the graphene lattice is broken, and only three of the six carbon atoms in each hexagonal ring is observed (Figure 4.5D). In comparison, the topograph taken on the same graphene sheet adjacent to the wrinkle (Figure 4.5E) reveals the honeycomb structure that is consistently observed on the “flat” (by “flat” we mean only the  $\sim 4$  Å ripples are present) parts of the monolayer graphene sheets investigated in our study. The “three-for-six” triangular patterns were observed on all ( $\sim 10$ ) the wrinkles we investigated over a couple of different graphene samples. For example, Figure 4.6 shows the triangular patterns observed on another wrinkle in another graphene sheet.

Most previous STM studies on monolayer graphene sheets on SiO<sub>2</sub> substrates reported honeycomb patterns.<sup>18-21</sup> Small ( $< 1$  nm) and random regions of “three-for-six” triangular patterns mixed with honeycomb patterns have been observed in one individual sample.<sup>17</sup> The origin of such patterns was unclear, but was conjectured to be due to the

presence of “strong spatially dependent perturbations”, including local curvature or trapped charges.<sup>17,43</sup> In our study, honeycomb patterns are observed for all “flat” parts of graphene (with  $\sim 4$  Å high ripples), while triangular patterns are exclusively and consistently observed on the  $\sim 3$  nm high wrinkles. These results indicate that increased local curvature (and the associated strain) on the wrinkles can provide strong enough perturbations to break the six-fold symmetry and degeneracy of the electronic states in graphene.

Because STM topographs represent the local density of states (DOS) distribution, we were able to further investigate how the “three-for-six” pattern characteristic of the wrinkles reflected the local electronic states and geometric structure of graphene.<sup>44</sup> This can be probed by measuring topographs at both positive and negative sample biases,<sup>44</sup> since such STM measurements will respectively probe the LUMO (empty states) and HOMO (filled states) of the sample.

Figure 4.6A, B gives the atomically resolved STM topographs of the top surface of a graphene wrinkle, obtained at positive and negative sample biases. The same “three-for-six” triangular patterns are observed for positive and negative biases (Figure 4.6C): the center parts of the two topographs, which correspond to the crest of the wrinkle, overlap with each other exactly, and a regular triangular lattice is observed. Small distortions of the triangular lattice are observed for regions away from the center, and the patterns obtained from the two scans gradually mismatch with each other. This suggests that the wrinkle is flexible, and the force from the STM tip causes a slight deformation of the wrinkle during scans. In comparison, on the “flat” part of the same graphene sheet (Figure 4.6D-F), although  $\sim 4$  Å ripples are present, clear honeycomb structures were

observed for both positive and negative biases, and the obtained topographs always exactly overlap, suggesting the ripples are more rigid compared to the wrinkle.

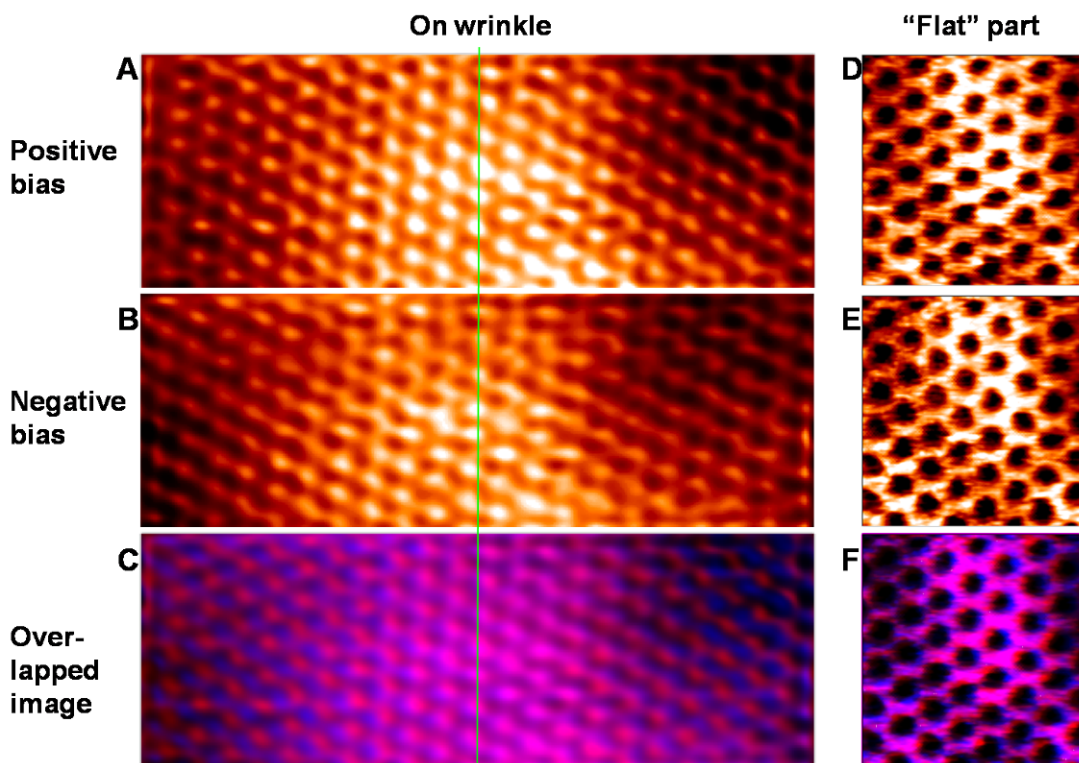


**Figure 4.6. Comparison of STM topographs of a graphene wrinkle and a “flat” part of the same graphene sheet, obtained at positive and negative sample biases. (A):** STM topograph (4.60 nm × 1.66 nm) of the top of a graphene wrinkle obtained at positive sample bias ( $V_b = 0.5$  V,  $I = 210$  pA). **(B):** STM topograph of the same region obtained at negative sample bias ( $V_b = -0.5$  V,  $I = -210$  pA). **(C):** An overlapped image, in which the topographs obtained at positive bias and negative bias are presented in red and blue, respectively. Overlapped regions thus become purple. The green line marks the center of the topograph, which is also the crest of the wrinkle. **(D):** STM topograph (1.5 nm × 1.5 nm) of a “flat” part of the same graphene sheet, obtained at positive sample bias ( $V_b = 0.5$  V,  $I = 150$  pA). **(E):** STM topograph of the same region obtained at negative sample bias ( $V_b = -0.5$  V,  $I = -150$  pA). **(F):** An overlapped image.

The same “three-for-six” patterns obtained on the wrinkle at positive and negative sample biases suggest the patterns reflect the actual topology of atoms in graphene. Recent experiments on hydrogenation of graphene have suggested that local bending/curvature in graphene may induce some  $sp^3$  hybridization component in the otherwise  $sp^2$ -hybridized carbons, which facilitates the breaking of delocalized  $\pi$ -bonds in graphene.<sup>45,46</sup> With a tendency towards  $sp^3$  hybridization, the six carbon atoms in each hexagon ring of graphene may start to adopt a structure similar to the chair conformation of cyclohexane, and so three of the six atoms protrude up and out of the hexagon ring, leading to the “three-for-six” pattern seen in our STM topographs.

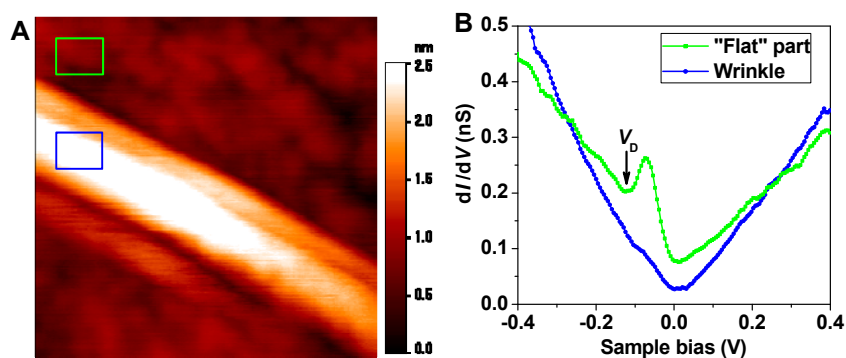


**Figure 4.7. Scanning tunneling spectroscopy study of a graphene wrinkle. (A):** Constant-current STM topograph (50 nm × 50 nm) of the wrinkle ( $V = 0.5$  V,  $I = 0.1$  nA). The largest height is  $\sim 3$  nm. **(B):** Differential conductance of the wrinkle [averaged over the blue rectangle in (A)], in comparison with that of a “flat” part [averaged over the green rectangle in (A)] of graphene, where ripples  $\sim 4$  Å in height are observed.

We have also characterized the electrical properties of graphene wrinkles through spatially resolved STS. Theoretical studies have suggested that corrugations and the associated strain in graphene may alter the local electrical properties of graphene.<sup>5, 14, 15</sup>

On the other hand, recent STS studies on graphene have found very limited or no correlations between corrugations and local electrical properties.<sup>21-23</sup> This is presumably because the previously studied ripples on “flat” parts of graphene were too small ( $\sim 4$  Å in height).

We have found distinctly different electrical properties for the  $\sim 3$  nm high wrinkles. Figure 4.7B presents the differential conductance behavior of a wrinkle, in comparison with other parts of the graphene sheet, where small ripples are present. Lower conductance is observed for the wrinkle at low bias voltages, indicating the wrinkle is less conductive than other parts of graphene. This is in agreement with our previous discussions that the local bending/curvature effects may weaken delocalized  $\pi$ -bonds. For the “flat” part of graphene, in addition to a soft gap at zero bias, a clear dip (local minimum) of differential conductance is observed at  $V_D = -0.12$  V (Figure 4.7B). This corresponds to the charge-neutral Dirac point of graphene,<sup>19</sup> at which energy the conduction and valance bands of graphene meet at a single point in  $k$ -space, and so charge carriers vanish. Interestingly, this dip disappears on the wrinkle (Fig 4.7B). This may be explained with recent theoretical studies, which suggest large local corrugations may lead to midgap states, and so a finite density of state is present at the neutrality point.<sup>14, 46, 47</sup>

We have utilized cryo-STM to investigate a new class of corrugations in monolayer graphene sheets, i.e., wrinkles  $\sim 10$  nm in width and  $\sim 3$  nm in height. We found such corrugations to be ubiquitous in graphene and have distinctly different properties in comparison to “flat” regions of graphene that only contain small ripples. The observed wrinkles are likely important for understanding the electrical and

mechanical properties of graphene. Recently developed graphene manipulation methods<sup>48,49</sup> may permit the controlled formation of wrinkles, which would be a first step toward harnessing wrinkles to control the electronic landscape of graphene sheets.

#### **4.4 Electron transport in graphene nanoribbons**

Figure 4.8 summarizes the conductance measurements as a function of gate voltage for three representative GNR devices of varying numbers of graphene layers (1, 2 and  $\sim 20$ ) but the same uniform width ( $W = 15 \pm 1$  nm). In our experiments, a heavily doped silicon substrate beneath the 300 nm SiO<sub>2</sub> surface layer was employed as the back gate. The measurements were performed at different temperatures as indicated. All curves exhibit a region of depressed conductance with respect to the gate voltage. As mentioned above, the carrier density in graphene vanishes at the Dirac point, where the conduction and valence bands meet. It is then expected in a low carrier density system that a dip in conductance would occur while tuning the carrier density by gating.<sup>27</sup> In an ideal, undoped device, this should occur at zero gate voltages. In our experiments, however, we often observe different minimal-conductance positions for different devices. Even for the same device, temperature cycling also often induces shifting of the minimal-conductance points and thus hysteresis. These shifts of the observed minimal-conductance points are due to the charges trapped in the underlying SiO<sub>2</sub> and possible adsorbates on top of graphene, which act as an electrostatic gate and modify the carrier types and densities accordingly.<sup>23</sup> For most of our devices, the minimal-conductance point occurs at positive gate voltages, indicating that they are p-type.

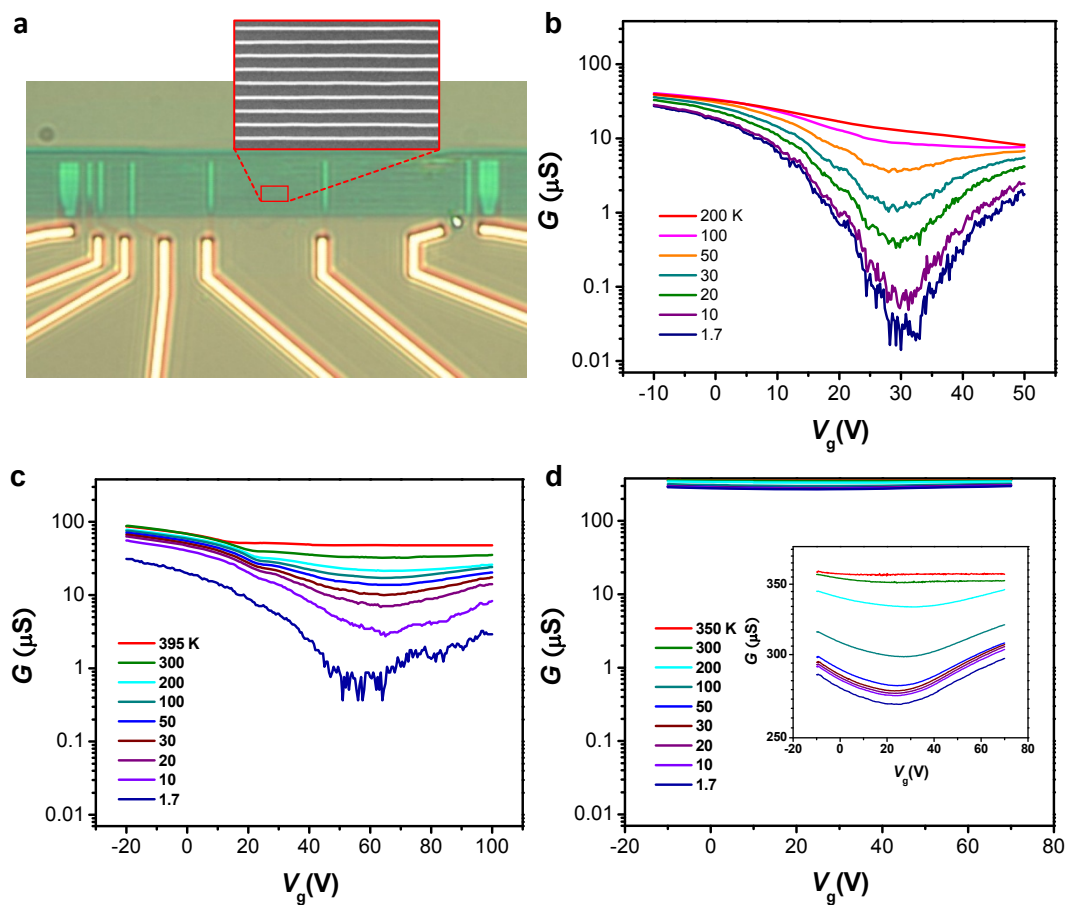


**Figure 4.8. Conductance measurements of graphene nanoribbons (GNRs).** (a) An optical image of a typical single-layer graphene FET device used in the transport measurements. The heavily doped silicon substrate beneath the 300 nm SiO<sub>2</sub> surface layer was used as the gate. Inset is an SEM micrograph of the GNRs (covered with SiO<sub>2</sub> and Pt wires). The width of the nanoribbon is measured to be 15 ± 1 nm; (b-d) Gate-voltage dependent conductance of single- (b), double- (c), and ~20-layer (d) GNRs measured at different temperatures; The numbers of parallel nanoribbons for (b-d) are 78, 65 and 45, respectively. The lengths of wires for (b-d) are 3, 12 and 2  $\mu\text{m}$ , respectively. Note that the conductance scales are the same for the three sets of devices. Inset in (d) is an expanded view of the same plot.

Our observations of a depressed region of conductance in GNRs are qualitatively in agreement with that in graphene films.<sup>25</sup> In “bulk” graphene, this dip corresponds to the minimum conductivity  $\sim 4e^2/h$ , where  $e$  and  $h$  are electron charge and Planck constant, respectively. At higher temperatures ( $>200\text{K}$ ), a similar behavior is observed in our GNR devices. For instance, at room temperature the single-layer GNR device gives a conductance dip (data not shown here) on the order of  $4e^2/h(nW/L)$ , where  $n$  and  $L$  are the number and length of parallel GNRs, respectively.

Remarkably, at low temperatures the minimum conductance decreases by more than an order of magnitude for both single- and double-layer GNRs, whereas the multi-layer device exhibits small decreases (Figure 4.8b-d). These results, i.e., conductance decreases with decreasing temperature regardless of the number of layers, indicate thermally activated behavior. This observed behavior is in general agreement with previous studies on *individual* GNRs, and suggests the opening up of band gaps in GNRs. In contrast, the conductance of bulk graphene films generally increases with decreasing temperature. However, it is noteworthy that in our study, the conductance gaps smoothly and consistently increase as temperature decreases for all GNR devices. This is in contrast to the large, ill-defined variations typically observed in previous studies on individual graphene nanoribbons.<sup>27, 29</sup> This is likely because we are measuring parallel GNRs, and so such sample-dependent variations are averaged out. Meanwhile, the more meaningful general trend becomes much clearer.

As the number of graphene layers increases, the temperature and gate-voltage dependence of conductance both weakens, suggesting smaller energy gaps in thicker GNRs. For the  $\sim 20$  layer GNRs in our study, the gap practically vanishes. This clear

observation that the band gap (and so the on-off ratio) decreases as the number of layers increases highlights the precisely controlled GNR width afforded by our SNAP technique. In contrast, previous experiments have not been able to tell the property differences between GNRs made of different numbers of layers, due to the difficulties in obtaining GNRs of well-defined widths.

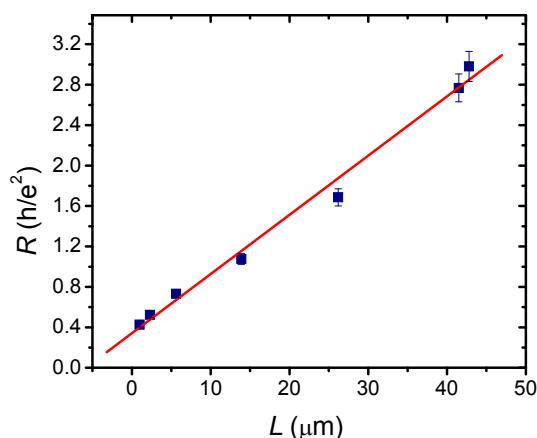


**Figure 4.9. Linear dependence of GNR resistance on ribbon length.** A plot of the resistance of single-layer graphene nanoribbons versus length, measured at room temperature with zero back-gate voltage. The number of ribbons in parallel is 78. Similar linear relationships were also observed for double- and multi-layer GNRs.

Figure 4.9 shows the total resistance of GNR arrays as a function of GNR length. A clear linear dependence is observed, which highlights the high quality of our GNRs with uniform properties. The small nonzero resistance at zero GNR length is likely due to the residue contact resistance which is independent of the ribbon length and can be subtracted from the curve. The hole mobility of our single-layer GNRs is estimated from the above back-gate FET measurements and plotted versus temperature in Figure 4.10a. The mobility slightly increases as the temperature drops from 200 K and peaks at about

25 K. The average value is slightly higher than previous studies ( $\sim 200 \text{ cm}^2/\text{Vs}$ ),<sup>29</sup> likely due to smoother edges of the GNR.

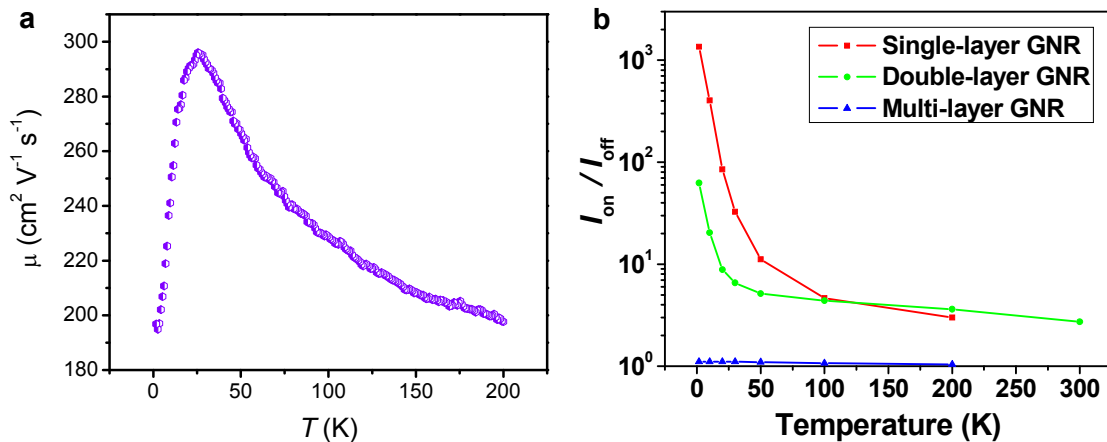


**Figure 4.10. Mobility and current on/off ratio analysis.** (a) Hole mobility versus temperature. The mobility data were extracted in the carrier density range:  $\sim 1.1\text{-}1.8 \times 10^{12} \text{ cm}^{-2}$ . (b)  $I_{\text{on}}/I_{\text{off}}$  versus temperature for various types of devices indicated.

Figure 4.10b summarizes our observation of the on-off current switching ratio ( $I_{\text{on}}/I_{\text{off}}$ ) for our GNR FET devices. For both single- and double-layer GNR FET devices, we observed a dramatic increase in  $I_{\text{on}}/I_{\text{off}}$  as the temperature decreases. Over 3 orders of magnitude in  $I_{\text{on}}/I_{\text{off}}$  was observed for the single-layer FET at temperature  $< 10$  K. This further suggests our GNRs are semiconducting and a band gap is induced. The energy gap could be extracted according to the thermally activated behavior of the GNR devices. The on-off current switching is proportional to  $\exp(E_g/k_B T)$ , where  $E_g$  is the gap energy.<sup>26</sup> We obtained an  $E_g$  of  $\sim 6.5$  and  $\sim 1.5$  meV for single- and double-layer graphene GNR FET devices respectively. According to an empirical form of  $E_g = \alpha/W$ ,<sup>25</sup> we obtained  $\alpha \sim 0.1$  eV nm. In recent density functional theory studies,<sup>50-52</sup> the energy gap is predicted

to be inversely proportional to the ribbon channel width, with a corresponding  $\alpha$  value ranging from 0.2-1.5 eV nm, which is largely consistent with our observation.

#### 4.5 Conclusion

In this chapter, we report on the scanning tunneling microscopy study of a new class of corrugations in exfoliated monolayer graphene sheets, i.e., wrinkles  $\sim 10$  nm in width and  $\sim 3$  nm in height. We found such corrugations to be ubiquitous in graphene, and have distinctly different properties when compared to other regions of graphene. In particular, a “three-for-six” triangular pattern of atoms is exclusively and consistently observed on wrinkles, suggesting the local curvature of the wrinkle provides a sufficient perturbation to break the six-fold symmetry of the graphene lattice. Through scanning tunneling spectroscopy, we further demonstrate that the wrinkles have lower electrical conductance and are characterized by the presence of midgap states, in agreement with recent theoretical predictions. The observed wrinkles are likely important for understanding the electrical properties of graphene.

We also studied the effect of width and number of graphene layers on the electronic transport in graphene nanoribbons (GNRs). As the lateral size decreases to nanometer range, conductance of *all* our GNR samples (regardless of number of layers) shows thermally activated behavior. Noticeable conductance gaps open up in both single- and double-layer GNR devices. The gaps smoothly and consistently increase as temperature decreases for all GNR devices. This contrasts with bulk graphene films, the conductance of which generally increases with decreasing temperature. Due to the precisely controlled GNR width afforded by SNAP, we have also for the first time clearly

observed how the properties of GNRs evolve as a function of number of layers: the band gap (and so the on-off ratio) decreases as the number of layers increases.

#### 4.6 References

1. Xu, K., Cao, P.G. & Heath, J.R. Scanning tunneling microscopy characterization of the electrical properties of wrinkles in exfoliated graphene monolayers. *Nano Lett.* **9**, 4446-4451 (2009).
2. Novoselov, K.S. et al. Electric field effect in atomically thin carbon films. *Science* **306**, 666-669 (2004).
3. Novoselov, K.S. et al. Two-dimensional atomic crystals. *Proc. Natl. Acad. Sci. U. S. A.* **102**, 10451-10453 (2005).
4. Geim, A.K. & Novoselov, K.S. The rise of graphene. *Nat. Mater.* **6**, 183-191 (2007).
5. Neto, A.H.C., Guinea, F., Peres, N.M.R., Novoselov, K.S. & Geim, A.K. The electronic properties of graphene. *Rev. Mod. Phys.* **81**, 109-162 (2009).
6. Geim, A.K. Graphene: status and prospects. *Science* **324**, 1530-1534 (2009).
7. Novoselov, K.S. et al. Room-temperature quantum hall effect in graphene. *Science* **315**, 1379-1379 (2007).
8. Mermin, N.D. Crystalline order in two dimensions. *Physical Review* **176**, 250-254 (1968).
9. Meyer, J.C. et al. The structure of suspended graphene sheets. *Nature* **446**, 60-63 (2007).
10. Meyer, J.C. et al. On the roughness of single- and bi-layer graphene membranes. *Solid State Commun.* **143**, 101-109 (2007).
11. Fasolino, A., Los, J.H. & Katsnelson, M.I. Intrinsic ripples in graphene. *Nat. Mater.* **6**, 858-861 (2007).
12. Morozov, S.V. et al. Strong suppression of weak localization in graphene. *Phys Rev Lett* **97**, 016801 (2006).
13. Morozov, S.V. et al. Giant intrinsic carrier mobilities in graphene and its bilayer. *Phys Rev Lett* **100**, 016602 (2008).
14. Guinea, F., Katsnelson, M.I. & Vozmediano, M.A.H. Midgap states and charge inhomogeneities in corrugated graphene. *Phys Rev B* **77**, 075422 (2008).
15. Kim, E.A. & Neto, A.H.C. Graphene as an electronic membrane. *Epl* **84**, 57007 (2008).
16. Herbut, I.F., Juricic, V. & Vafek, O. Coulomb interaction, ripples, and the minimal conductivity of graphene. *Phys Rev Lett* **100**, 046403 (2008).

17. Ishigami, M., Chen, J.H., Cullen, W.G., Fuhrer, M.S. & Williams, E.D. Atomic structure of graphene on SiO<sub>2</sub>. *Nano Lett.* **7**, 1643-1648 (2007).
18. Stolyarova, E. et al. High-resolution scanning tunneling microscopy imaging of mesoscopic graphene sheets on an insulating surface. *Proc. Natl. Acad. Sci. U. S. A.* **104**, 9209-9212 (2007).
19. Zhang, Y.B. et al. Giant phonon-induced conductance in scanning tunnelling spectroscopy of gate-tunable graphene. *Nat. Phys.* **4**, 627-630 (2008).
20. Geringer, V. et al. Intrinsic and extrinsic corrugation of monolayer graphene deposited on SiO<sub>2</sub>. *Phys Rev Lett* **102**, 076102 (2009).
21. Deshpande, A., Bao, W., Miao, F., Lau, C.N. & LeRoy, B.J. Spatially resolved spectroscopy of monolayer graphene on SiO<sub>2</sub>. *Phys Rev B* **79**, 205411 (2009).
22. Teague, M.L. et al. Evidence for strain-induced local conductance modulations in single-layer graphene on SiO<sub>2</sub>. *Nano Lett.* **9**, 2542-2546 (2009).
23. Zhang, Y., Brar, V.W., Girit, C., Zettl, A. & Crommie, M.F. Origin of spatial charge inhomogeneity in graphene. *Nat. Phys.* **5**, 722-726 (2009).
24. Han, M.Y., Brant, J.C. & Kim, P. Electron transport in disordered graphene nanoribbons. *Phys Rev Lett* **104**, 056801 (2010).
25. Han, M.Y., Ozyilmaz, B., Zhang, Y.B. & Kim, P. Energy band-gap engineering of graphene nanoribbons. *Phys Rev Lett* **98**, 206805 (2007).
26. Li, X.L., Wang, X.R., Zhang, L., Lee, S.W. & Dai, H.J. Chemically derived, ultrasmooth graphene nanoribbon semiconductors. *Science* **319**, 1229-1232 (2008).
27. Chen, Z.H., Lin, Y.M., Rooks, M.J. & Avouris, P. Graphene nano-ribbon electronics. *Physica E* **40**, 228-232 (2007).
28. Jiao, L.Y., Zhang, L., Wang, X.R., Diankov, G. & Dai, H.J. Narrow graphene nanoribbons from carbon nanotubes. *Nature* **458**, 877-880 (2009).
29. Wang, X.R. et al. Room-temperature all-semiconducting sub-10-nm graphene nanoribbon field-effect transistors. *Phys Rev Lett* **100**, 206803 (2008).
30. Bai, J.W., Duan, X.F. & Huang, Y. Rational fabrication of graphene nanoribbons using a nanowire etch mask. *Nano Lett.* **9**, 2083-2087 (2009).
31. Sols, F., Guinea, F. & Neto, A.H.C. Coulomb blockade in graphene nanoribbons. *Phys Rev Lett* **99**, 166803 (2007).
32. Martin, I. & Blanter, Y.M. Transport in disordered graphene nanoribbons. *Phys Rev B* **79**, 235132 (2009).

33. Zhang, Y.B., Tan, Y.W., Stormer, H.L. & Kim, P. Experimental observation of the quantum Hall effect and Berry's phase in graphene. *Nature* **438**, 201-204 (2005).
34. Ferrari, A.C. et al. Raman spectrum of graphene and graphene layers. *Phys Rev Lett* **97**, 187401 (2006).
35. Graf, D. et al. Spatially resolved Raman spectroscopy of single- and few-layer graphene. *Nano Lett.* **7**, 238-242 (2007).
36. Melosh, N.A. et al. Ultrahigh-density nanowire lattices and circuits. *Science* **300**, 112-115 (2003).
37. Rutter, G.M. et al. Scattering and interference in epitaxial graphene. *Science* **317**, 219-222 (2007).
38. Cerda, E. & Mahadevan, L. Geometry and physics of wrinkling. *Phys Rev Lett* **90**, 074302 (2003).
39. Biedermann, L.B., Bolen, M.L., Capano, M.A., Zemlyanov, D. & Reifenberger, R.G. Insights into few-layer epitaxial graphene growth on 4H-SiC(0001) substrates from STM studies. *Phys Rev B* **79**, 125411 (2009).
40. Li, X.S. et al. Large-area synthesis of high-quality and uniform graphene films on copper foils. *Science* **324**, 1312-1314 (2009).
41. Chang, H.P. & Bard, A.J. Observation and characterization by scanning tunneling microscopy of structures generated by cleaving highly oriented pyrolytic-graphite. *Langmuir* **7**, 1143-1153 (1991).
42. Guinea, F., Horovitz, B. & Le Doussal, P. Gauge fields, ripples and wrinkles in graphene layers. *Solid State Commun.* **149**, 1140-1143 (2009).
43. Stolyarova, E. et al. Scanning tunneling microscope studies of ultrathin graphitic (graphene) films on an insulating substrate under ambient conditions. *J Phys Chem C* **112**, 6681-6688 (2008).
44. Kane, C.L. & Mele, E.J. Broken symmetries in scanning tunneling images of carbon nanotubes. *Phys Rev B* **59**, R12759-R12762 (1999).
45. Ryu, S. et al. Reversible basal plane hydrogenation of graphene. *Nano Lett.* **8**, 4597-4602 (2008).
46. Elias, D.C. et al. Control of graphene's properties by reversible hydrogenation: evidence for graphane. *Science* **323**, 610-613 (2009).
47. Wehling, T.O., Balatsky, A.V., Tsvelik, A.M., Katsnelson, M.I. & Lichtenstein, A.I. Midgap states in corrugated graphene: Ab initio calculations and effective field theory. *Epl* **84**, 17003 (2008).

48. Bao, W. et al. Controlled ripple texturing of suspended graphene and ultrathin graphite membranes. *Nature Nanotechnology* **4**, 562-566 (2009).
49. Li, Z., Cheng, Z., Wang, R., Li, Q. & Fang, Y. Spontaneous formation of nanostructures in graphene. *Nano Lett.* **9**, 3599-3602 (2009).
50. Son, Y.W., Cohen, M.L. & Louie, S.G. Energy gaps in graphene nanoribbons. *Phys Rev Lett* **97**, 216803 (2006).
51. Son, Y.W., Cohen, M.L. & Louie, S.G. Half-metallic graphene nanoribbons. *Nature* **444**, 347-349 (2006).
52. Barone, V., Hod, O. & Scuseria, G.E. Electronic structure and stability of semiconducting graphene nanoribbons. *Nano Lett.* **6**, 2748-2754 (2006).